

# Near-infrared organic light-emitting diodes with very high external quantum efficiency and radiance

Kiet Tuong Ly<sup>1</sup>, Ren-Wu Chen-Cheng<sup>2</sup>, Hao-Wu Lin<sup>2\*</sup>, Yu-Jeng Shiau<sup>2</sup>, Shih-Hung Liu<sup>3</sup>, Pi-Tai Chou<sup>3\*</sup>, Cheng-Si Tsao<sup>4,5</sup>, Yu-Ching Huang<sup>4</sup> and Yun Chi<sup>1\*</sup>

**Bright and efficient organic emitters of near-infrared light would be of use in applications ranging from biological imaging and medical therapy to night-vision devices. Here we report how a new class of Pt(II) complex phosphors have enabled the fabrication of organic light-emitting diodes that emit light at 740 nm with very high efficiency and radiance due to a high photoluminescence quantum yield of ~81% and a highly preferred horizontal dipole orientation. The best devices exhibited an external quantum efficiency of  $24 \pm 1\%$  in a normal planar organic light-emitting diode structure. The incorporation of a light out-coupling hemisphere structure further boosts the external quantum efficiency up to  $55 \pm 3\%$ .**

Phosphorescent metal complexes have attracted increasing interest because of their intriguing fundamental chemical and photophysical properties, as well as commercial applications in organic light-emitting diodes (OLEDs) for flat panel displays and lighting luminaires. Both the metal element and the design of the ligating ancillaries have a profound influence on the structural and electronic properties of the OLED. Although the majority of phosphorescent metal complexes exhibit vivid visible emission spanning from blue to red, another key class of functional phosphors is the near-infrared (NIR) emitters, that is, those with emission peak wavelengths beyond 700 nm (ref. 1), which is of great importance for applications in optical signal processing<sup>2</sup>, night-vision technologies<sup>3</sup>, bioimaging<sup>4</sup> and photodynamic therapy<sup>5</sup>. In contrast to designs using donor-acceptor organics<sup>6,7</sup>, for which intramolecular charge transfer (ICT) between the constituent groups results in the observed NIR emission, the emission bandgap can be also fine-tuned to the NIR regime by employing transition metal-based complexes<sup>8</sup>.

Despite the great potential for applications, however, the development of efficient NIR emitters has long been hampered by their much lower emission efficiency compared with that of visible emitters. One intrinsic quenching mechanism, commonly dubbed the 'energy gap law', specifies that in the absence of a zero-order surface crossing, the deactivation pathway between the lowest lying singlet ( $S_1$ ) or triplet ( $T_1$ ) states and the ground state ( $S_0$ ) can be facilitated by coupling between the zero vibration level of the  $S_1$  (or  $T_1$ ) state and the higher vibration levels of the  $S_0$  state. This nonradiative process is greatly enhanced if the emission gap decreases, particularly when the gap is near the NIR region<sup>9,10</sup>.

From a fundamental perspective, one feasible way to suppress this quenching process is to reduce the vibrational overlap<sup>11</sup>. Accordingly, perdeuterated or perfluorinated approaches have been employed to decrease the number of high-frequency vibrations associated with C-H, O-H and N-H stretching; however, this strategy is synthetically formidable and not cost-effective. Moreover, this approach results in only partial or even negligible improvements

due to the retention of many other vibrational modes and their combinations. Alternatively, if the transition to the ground state possesses a shallow or even repulsive potential energy surface (PES) in the ground state, high-frequency vibrational quenching may theoretically be significantly reduced. The creation of such a PES may be realized by the formation of an excimer (or excited oligomer), for example, in which there are small or negligible interactions between individual molecules in the ground state, but dimers or oligomers form on excitation. Owing to the shallow, repulsive-like PES in the ground state, the excimer emission is subject to less vibrational quenching imposed by the energy gap law.

## Conceptual design

For Pt(II) phosphors, the extended  $\pi$  conjugation of the peripheral chelate may serve as a key factor in inducing the  $\pi$ - $\pi$  stacking interaction between square-planar motifs to achieve longer-wavelength emission. More importantly, the metal-metal-to-ligand charge transfer (MMLCT) transition character<sup>12,13</sup> fulfils the requirement for a shallow and/or repulsive PES in the ground state<sup>14</sup>. Consequently, a number of efficient NIR-emitting OLEDs that are based on Pt(II) complexes have been recognized<sup>15-26</sup>. The most efficient NIR OLED reported<sup>27</sup> has an emission peak at ~700 nm and a maximum external quantum efficiency (EQE) of 14.5%. Moreover, NIR emission with a peak maximum at 773 nm and an EQE of 9.2% has been reported for the tetrabenzoporphyrin Pt(II) complex with bulky 3,5-di-*tert*-butylphenyl substituents<sup>28</sup>. In this study we report a giant step forwards in the fabrication of NIR-emitting OLEDs. By strategically designing and synthesizing a new series of 2-pyrazinyl pyrazolate Pt(II) complexes, we obtained 740 nm OLEDs with a peak EQE of  $24 \pm 1\%$  and radiance of  $(3.6 \pm 0.2) \times 10^5$  mW sr<sup>-1</sup> m<sup>-2</sup> in a normal planar OLED structure. The high absolute thin-film photoluminescence quantum yields (PLQY,  $\Phi$ ) and highly preferred horizontal oriented dipoles of these Pt(II) complexes both contributed to these high efficiencies<sup>29</sup>. Previous studies have shown that if high-resolution images are not needed, such as in OLED lighting, the incorporation of a light out-coupling hemisphere structure

<sup>1</sup>Department of Chemistry, National Tsing Hua University, Hsinchu 30013, Taiwan. <sup>2</sup>Department of Materials Science and Engineering, National Tsing Hua University, Hsinchu 30013, Taiwan. <sup>3</sup>Department of Chemistry, National Taiwan University, Taipei 10617, Taiwan. <sup>4</sup>Institute of Nuclear Energy Research, Taoyuan 32546, Taiwan. <sup>5</sup>Department of Materials Science and Engineering, National Taiwan University, Taipei 10617, Taiwan.

\*e-mail: hmlin@mx.nthu.edu.tw; chop@ntu.edu.tw; ychi@mx.nthu.edu.tw

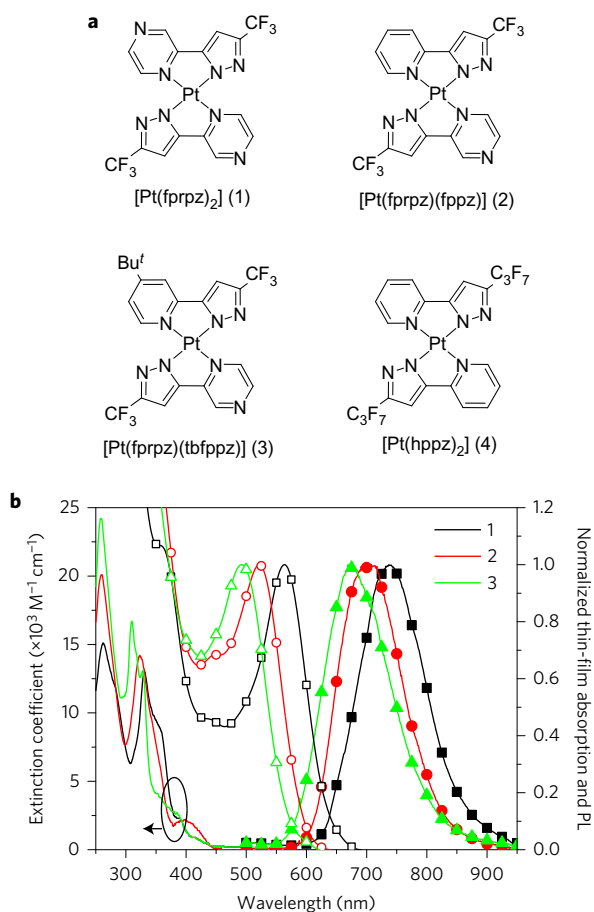


**Figure 1 | Chemical structure and optical properties of Pt(II) complexes 1-3.**

**a.** Pt(II) complexes 1-3. Structurally characterized [Pt(hppz)<sub>2</sub>] (4), whose packing arrangement was used to simulate the dimer and trimer of 1 in the solid state<sup>35</sup> is also shown. **b.** The absorption spectra of 1-3 in THF. The corresponding absorption (unfilled symbols, righthand y axis) and emission spectra in solid film (filled symbols, righthand y axis) normalized at the peak wavelength are also shown.

can effectively enhance the extraction efficiency by more than twofold<sup>30-32</sup>. The integration of this gadget further increased the EQE to  $55 \pm 3\%$ . Both achievements represent landmarks in the history of NIR OLEDs.

### Chemistry and photophysics

The homoleptic [Pt(fprpz)<sub>2</sub>] (1) was synthesized by treating Pt(DMSO)<sub>2</sub>Cl<sub>2</sub> with two equivalents of 2-pyrazinyl pyrazole (that is, fprpzH) in tetrahydrofuran (THF) and three equivalents of Na<sub>2</sub>CO<sub>3</sub>. Alternatively, the heteroleptic pyrazinyl pyrazolate Pt(II) complexes were synthesized using an equal molar ratio of a Pt(LH)Cl<sub>2</sub> intermediate<sup>33</sup> (LH = 2-pyridyl pyrazole (fppzH)), 2-(4-*t*-butylpyridyl) pyrazole (tbfppzH) and fprpzH in refluxing 2-methoxyethanol for 16 h. After removal of the solvent, the residue was sublimed under a high vacuum to produce the analytically pure Pt(II) complexes 1, [Pt(fprpz)(fppz)] (2) and [Pt(fprpz)(tbfppz)] (3) (see Fig. 1a). All complexes exhibited good solubility in THF and toluene compared with solvents such as acetone, CH<sub>2</sub>Cl<sub>2</sub> and dimethylsulfoxide (DMSO).

The absorption spectra in THF and emission of the corresponding 2-pyrazinyl pyrazolate Pt(II) complexes in solid film are shown in Fig. 1b; pertinent numerical data are listed in Table 1. The lower-lying absorption band, with peak wavelengths at 397 nm (1), 387 nm (2) and 328 nm (3), was assigned to the metal-ligand charge transfer (MLCT) transition (see below). Emission spectra

indicated that these Pt(II) complexes were non-emissive in both the aerated and degassed fluid states at room temperature, but exhibited highly intense emission in both fine powder and vacuum-deposited thin film. The PL spectra of solid-state thin films revealed emission peaks at 740, 703 and 673 nm; these spectral features are the mirror images of the corresponding absorption spectra with maxima at 563, 522 and 494 nm for complexes 1-3, respectively (see Fig. 1b). Note that the absorption in the thin solid film was substantially redshifted compared with the absorption observed in the THF solution (397, 387 and 328 nm), consistent with the MMLCT character observed in many square-planar Pt(II) metal complexes that exhibit prominent solid-state aggregation. The absolute thin-film PLQY of complexes 1-3 were as high as 81, 55 and 82% and were thus considerably higher than all other reported NIR compounds. These high PLQY values and the population lifetimes, which were 313, 365 and 309 ns, imply radiative lifetimes of 386, 663 and 377 ns for complexes 1-3, respectively. The high NIR PLQY for these Pt(II) pyrazolate complexes is attributable to the submicrosecond radiative lifetime of the MMLCT process in the triplet manifold and excitonic character. Further details are provided in the Computational methods section of the Methods.

### Solid-state packing

The synchrotron X-ray diffraction results clearly revealed an ordered aggregation of these 2-pyrazinyl Pt(II) complexes in the vacuum-evaporated thin films. Grazing-incidence wide-angle X-ray scattering (GIWAXS) was performed to investigate the crystal structure, orientation and molecular packing of thin-film crystal<sup>34</sup>. Figure 2a-c shows the two-dimensional (2D) GIWAXS patterns of the films derived from complexes 1-3. Films of Pt(II) complexes 1 and 2 exhibited a single-crystal-like GIWAXS pattern with an ordered crystal orientation. The lattice parameters and structure of these crystalline thin films resembled those of thin films previously reported in the literature<sup>29</sup>. For clarity, Fig. 2d schematically illustrates the 3D ordered packing arrangement of complex 1. The main crystal orientation was indicated by the strongest (200) diffraction spots along the out-of-plane direction ( $Q_z$  in Fig. 2a), which revealed the (100) plane parallel to the film (substrate) surface. This preferred orientation had edge-on molecular ordering lying on the (100) plane. The GIWAXS pattern of thin film 3 indicates a much less ordered structure (mainly 2D lamellar structure) but the same edge-on orientation. The crystallinity ratios of films 1-3 determined by the integrated intensity of the (200) diffraction peak were 1:1.76:0.35, respectively. The azimuthally angular distribution of (200) spots (Supplementary Fig. 1) revealed that ~90% of the crystals had a tilt angle of less than 10° in the films. The lattice parameters along the [100] direction of films 1-3 determined by the peak width were 18.5, 19.3 and 18.5 nm, respectively. According to the GIWAXS patterns, the spacing between the (100) planes of films 1-3 was calculated to be 2.24, 2.20 and 2.71 nm, respectively. The interspacing between the (010) planes of films 1 and 2 was 1.22 nm.

The above molecular aggregation in the vacuum-deposited thin films resulted in an uneven transition dipole distribution. To further investigate the emission dipole orientation, an angle-dependent PL intensity measurement was performed in which the *P*-polarized light was selected by an optical polarizer and the measured wavelength was ~740 nm for 1, ~683 nm for 2 and ~670 nm for 3. Supplementary Fig. 2 shows the angle-dependent PL intensity of 30-nm thin films. The horizontal dipole ratio ( $\Theta$ ) was calculated to be 0.87, 0.88 and 0.77 for films 1-3, respectively, thus indicating that complexes 1 and 2 possessed a similar emission dipole orientation distribution and tended to lie horizontally on the substrate surface. Despite relatively randomly distributed dipoles, complex 3 still exhibited a preferred horizontal orientation on average. The horizontal orientation of the transition dipoles effectively stimulates the emission light to couple

**Table 1 | Photophysical properties of Pt(II) complexes 1-3.**

Pt(II) complex	Absorption $\lambda_{\max}$ (nm) ( $\epsilon \times 10^{-3} \text{ M}^{-1} \text{ cm}^{-1}$ ) <sup>a</sup>	Emission $\lambda_{\max}$ (nm) <sup>†</sup>	$\Phi$ (%) <sup>†</sup>	$\tau$ (ns) <sup>‡</sup>	$k_r$ (s <sup>-1</sup> ) <sup>§</sup>	$k_{nr}$ (s <sup>-1</sup> ) <sup>§</sup>
1	330 (13), 387 (2.3)	740	81	313	$2.59 \times 10^6$	$6.02 \times 10^5$
2	322 (14.2), 397 (2.2)	703	55	365	$1.50 \times 10^6$	$1.24 \times 10^6$
3	328 (13.1), 385 (2.7)	673	82	309	$2.65 \times 10^6$	$5.91 \times 10^5$

<sup>a</sup>UV-visible spectra were recorded in a THF solution at a concentration of  $10^{-5}$  M; the numbers in parentheses stand for the extinction coefficient,  $\epsilon$ . <sup>†</sup>PLQY values were measured on the film at room temperature; <sup>‡</sup>PL lifetime ( $\tau$ ) data were measured using a sublimed powder sample; <sup>§</sup>radiative decay rate constant ( $k_r$ ) and non-radiative decay rate constant ( $k_{nr}$ ) were calculated according to the equations  $k_r = \Phi/\tau_{\text{obs}}$  and  $k_{nr} = (1/\tau_{\text{obs}}) - k_r$ , respectively.

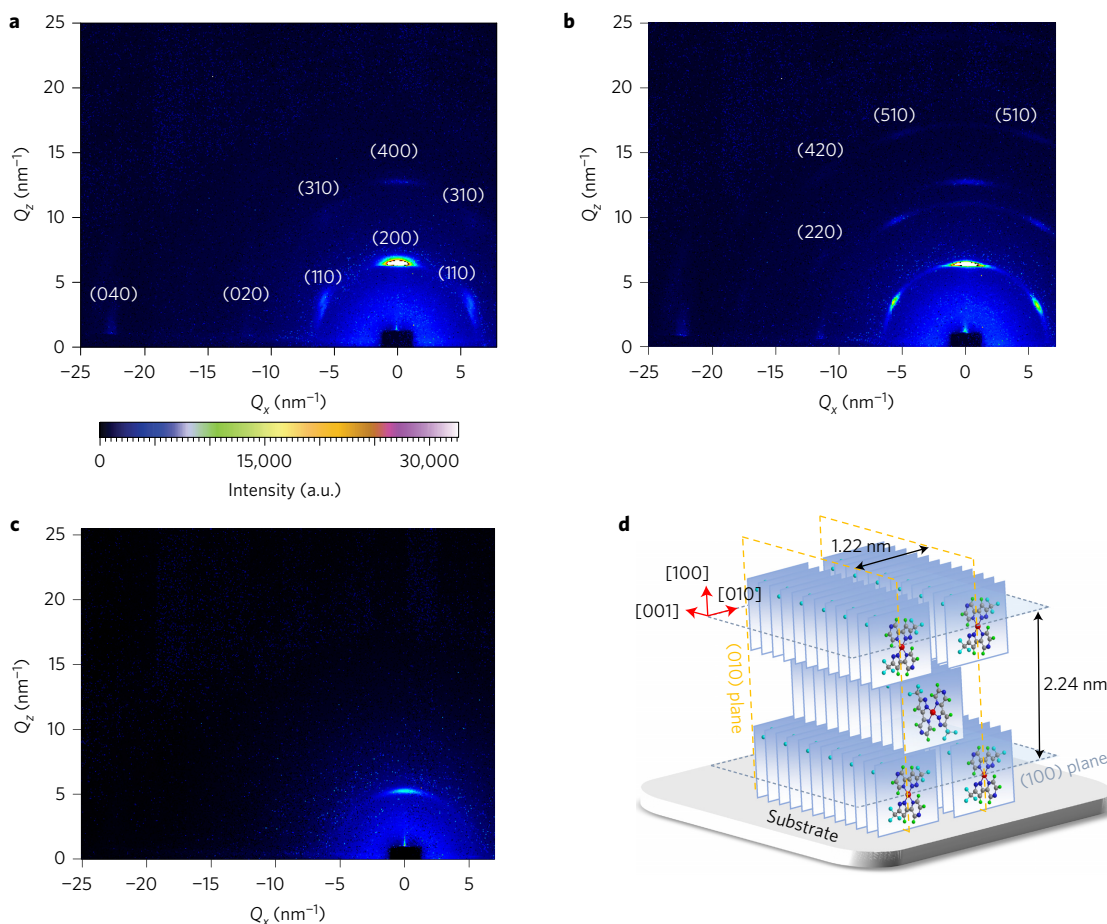


**Figure 2 | GIWAXS data for thin films of Pt(II) complexes 1-3.** **a-c**, 2D GIWAXS diffraction patterns of the vacuum-deposited thin films of complexes 1-3, respectively. **d**, Schematic illustration of the 3D ordered packing of complex 1 on the substrate surface.

to the air mode, consistent with the observed high efficiency of the OLED devices presented in the subsequent section.

### Theoretical investigation

We then employed a computational time-dependent density functional theory (TD-DFT) approach to gain in-depth insight into the self-assembly and MMLCT properties of these 2-pyrazinyl Pt(II) complexes at the molecular level (see Supplementary Information for details of the computational methodology). The calculated singlet and triplet absorption characteristics for monomeric Pt(II) complexes 1-3 are displayed in Supplementary Tables 1-3 and Figs 3-5. The calculated wavelengths of the lowest singlet optical absorption ( $S_0 \rightarrow S_1$ ) of 434.9 nm for 1, 418.6 nm for 2 and 418.2 nm for 3 are close to the observed onsets of the absorption peaks shown in Fig. 1. The  $S_0 \rightarrow S_1$  for 1-3 is assigned to the transition from the highest occupied molecular orbital to the lowest unoccupied molecular orbital (HOMO  $\rightarrow$  LUMO), in which the HOMO and LUMO are mainly localized at the Pt(II)

centre and  $\pi^*$  orbital of the chelates, respectively, consistent with a contribution from the typical MLCT transition.

We then further probed self-assembly in the solid state. Owing to the strong aggregation along the  $d_z$  direction, attempts to grow single crystals of complexes 1-3 failed. As an alternative, we applied the scaffold of a closely related Pt(II) complex, [Pt(hppz)<sub>2</sub>] (4) (Fig. 1a), which bears similar pyrazolate ligands with known X-ray structures, and then extended the framework to the dimeric form<sup>35</sup>. In this approach, we started by squeezing the Pt-Pt distance of the dimer. We then conducted unrestricted geometric optimization of the Pt-Pt distance and obtained both the  $S_1$  and  $T_1$  states. The results for 1 shown in Supplementary Fig. 6 indicate that independent of the starting Pt-Pt distance within a large range of 2.60 Å - 3.15 Å, the Pt-Pt distance of the optimized geometry resulted in 2.936 Å and 2.928 Å for the  $S_1$  and  $T_1$  states, with estimated  $S_1 \rightarrow S_0$  and  $T_1 \rightarrow S_0$  energy gaps (in terms of wavelength) of 587 and 617 nm, respectively (Supplementary Table 4). The 617 nm for the  $T_1 \rightarrow S_0$  transition is higher in energy than the phosphorescence at 740 nm

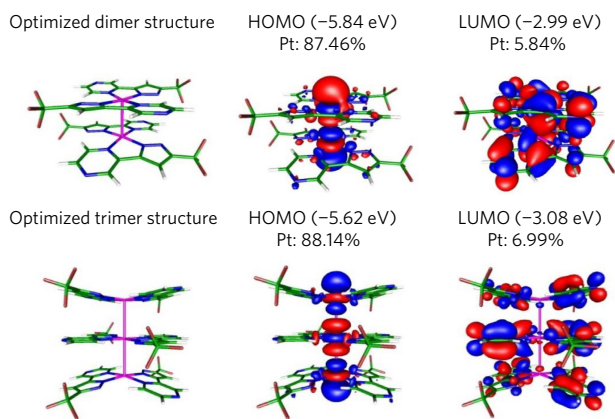


**Figure 3 | Molecular orbitals of Pt(II) complex 1.** Frontier molecular orbitals of HOMO and LUMO in the  $T_1$  state for Pt(II) complex 1 and the percentage of the electron density from the Pt atoms for the dimer (top) and trimer (bottom) configurations. Red and blue represent two different phases of orbitals.

for complex 1 in the solid film state. To mimic the situation en route to aggregation, we then extended the calculation to a trimeric configuration of 1 under full geometry optimization in both the  $S_1$  and  $T_1$  states. The resulting Pt–Pt distances were calculated as (3.20 Å, 3.20 Å) and (3.14 Å, 3.15 Å) for  $S_1$  and  $T_1$ , with  $S_1 \rightarrow S_0$  and  $T_1 \rightarrow S_0$  energy gaps of 605 and 694 nm, respectively. The latter (694 nm) is much closer to the observed phosphorescence at 740 nm, supporting the aggregation property via  $d_{z^2}$  and/or  $\pi$  interaction. Further extension to the tetramer or even oligomer is unfortunately limited by the current computation capacity.

Figure 3 reveals that the frontier molecular orbitals for HOMO and LUMO contributed to the dimer (top) and trimer (bottom) in the  $T_1$  state of complex 1 (see Supplementary Fig. 7 and Supplementary Table 4 for other associated frontier orbitals contributing to the  $S_1$  state). For complexes 2 and 3, the associated frontier orbitals and emission characters that contribute to the  $S_1$  and  $T_1$  excited states for dimer and trimer excimers are also displayed in Supplementary Figs 8 and 9 and Supplementary Tables 5 and 6. As the assembly increases from monomer to dimer and then to trimer in the  $T_1$  state of complex 1, the contribution of the  $d_{z^2}$  orbital in HOMO increases from 32.03 to 88.14%. A dominant  $d_{z^2}$  contribution in the HOMO is thus expected on expanding the aggregation to infinity. The LUMO is located mainly at the ligand  $\pi^*$  orbitals on aggregation. Such an MMLCT property along the linear Pt–Pt linkage can be recognized as an exciton-like model. Owing to the short stacking distance, the interaction among  $5d_{z^2}$  (HOMO) and among ligand  $\pi^*$  orbitals (LUMO) is expected to be strong. Therefore, the exciton, after being created, may have a long diffusion length and hence be much less susceptible to exciton–optical phonon coupling, which is also conventionally referred to as exciton–vibrational coupling at the molecular level<sup>36,37</sup>. Therefore, the influence of the energy gap law can be suppressed, thus permitting the anomalously high NIR emission yield ( $\sim 740$  nm, QY  $\approx 81\%$ ) of complex 1 and its analogues.

### Device characterization

The OLED devices consisted of a layered architecture of glass/indium tin oxide (ITO) (100 nm)/1,4,5,8,9,11-hexaazatriphenylene hexacarbonitrile (HATCN) (10 nm)/N,N'-bis(naphthalen-1-yl)-N,N'-bis(phenyl)benzidine (NPB) (50 nm)/1,3-bis(N-carbazolyl)benzene (mCP) (15 nm)/Pt(II) emitter (20 nm)/2,2',2''-(1,3,5-benzinetriyl)-tris(1-phenyl-1-H-benzimidazole) (TPBi) (60 nm)/8-hydroxyquinolalithium (LiQ) (2 nm)/Al (100 nm) in which HATCN, NPB, TPBi and LiQ were the hole-injecting material, hole-transporting layer (HTL), electron-transporting layer (ETL)

and electron-injecting layer (EIL), respectively. The device structure and material energy band diagram are shown in Supplementary Fig. 10. The thicknesses of the HTL and ETL were also adjusted to attain the optimal carrier transports. Owing to the much-stabilized HOMO and LUMO of the studied Pt(II) complexes (Supplementary Table 7), mCP played a critical role in eliminating the non-emissive exciplex formation between NPB and the Pt(II) complexes. Taking 1 as an example, the HOMO and LUMO resided at  $-6.01$  eV and  $-3.85$  eV, respectively. The holes injected from NPB (with HOMO =  $-5.5$  eV and LUMO =  $-2.4$  eV) were blocked at the interface in the absence of mCP and eventually recombined with electrons from the LUMO of the Pt complexes, resulting in a non-emissive exciplex and inferior performance, as shown in Supplementary Fig. 11. These devices exhibited electroluminescent (EL) spectra with a peak maximum at  $\sim 900$  nm; the EL spectra varied with different ETL thicknesses, possibly owing to the shifting of carrier recombination zones. The optimized EQE of these devices was only 0.0034%.

However, with the insertion of an mCP layer between the NPB and EML, highly intense EL spectra were observed for all OLED devices. Their emission peak maxima were located at  $\sim 740$ ,  $\sim 683$  and  $\sim 670$  nm, respectively, revealing spectral features similar to those of PL (see Table 1 and Supplementary Fig. 12). Both the current density–voltage–radiance characteristics ( $J$ – $V$ – $R$ ) and EQE and power conversion efficiencies (PCE), as a function of brightness, are shown in Fig. 4. All device performance parameters are summarized in Supplementary Table 8. The low leakage currents and  $J$ – $V$ – $R$  characteristics indicated smooth thin-film morphologies despite the higher crystallinity. The maximum EQE values were  $24 \pm 1\%$ ,  $21 \pm 1\%$  and  $24 \pm 1\%$  for complexes 1–3, respectively. The  $24 \pm 1\%$  EQE of device 1 is the highest reported value for an NIR OLED so far; the emission wavelength ( $\lambda_{\max} = 740$  nm) was substantially redshifted compared with the previous red–NIR OLED result<sup>27</sup> (EQE = 14.5%,  $\lambda_{\max} = 700$  nm). Hence, the EL emission of device 1 consisted of 78% of  $\geq 700$  nm NIR emission versus the  $\sim 50\%$  NIR irradiation (see Table 1)<sup>27</sup>. Furthermore, compared with a pure NIR device<sup>28</sup> ( $\lambda_{\max} = 773$  nm), device 1 exhibited a twofold improvement in NIR efficiency ( $19 \pm 1\%$  versus 9.2%). More importantly, the highest NIR radiance for device 1 was  $\sim 20$  times higher than that of the pure NIR devices<sup>28</sup>:  $(2.8 \pm 0.2) \times 10^5$  mW sr<sup>-1</sup> m<sup>-2</sup> versus  $0.14 \times 10^5$  mW sr<sup>-1</sup> m<sup>-2</sup>.

These high device performances can be attributed to the high thin-film QY as well as the horizontal orientation of the emission dipoles. To quantify the effect of the emission dipole orientation on out-coupling efficiency ( $\eta_{\text{out}}$ ) of the OLED, optical simulations were performed. The model used in the simulation adopted classical oscillating electrical dipole to represent the molecular transition dipole moments. The full-vectorial plane-wave expansion of the dipole field was calculated and the far-field radiation air-mode ( $\Phi_{\text{air}}$ ) can thus be obtained<sup>38,39</sup>. If the emission dipoles were isotropically oriented, the calculated out-coupling efficiencies are estimated to be 22, 23 and 25% for devices 1, 2 and 3, respectively, whereas perfect horizontally oriented dipoles deliver much higher out-coupling efficiencies of 34, 36 and 36%, respectively. Given the horizontal dipole ratios ( $\Theta$ , see Supplementary Fig. 2) in thin films 1–3 obtained from angle-dependent PL analysis (0.87, 0.88 and 0.77), the out-coupling efficiencies of devices 1–3 were estimated to be 30, 31 and 28%, respectively. Supplementary Fig. 13 shows the calculated  $\Phi_{\text{air}}$  as a function of the HTL and ETL thicknesses for device 1. The simulation indicates that the experimental device structure was in nearly optimized optical condition. By multiplying the QY of thin film 1 ( $\sim 81\%$ ) and the theoretical out-coupling efficiency (30%), the calculated EQE is 24%, which is in good agreement with the experimentally obtained EQE value of  $24 \pm 1\%$ .

Incorporating a light out-coupling hemisphere structure with the devices was known to be an effective way to couple out the substrate modes ( $\Phi_{\text{sub}}$ ) from the devices, giving an approximately twofold

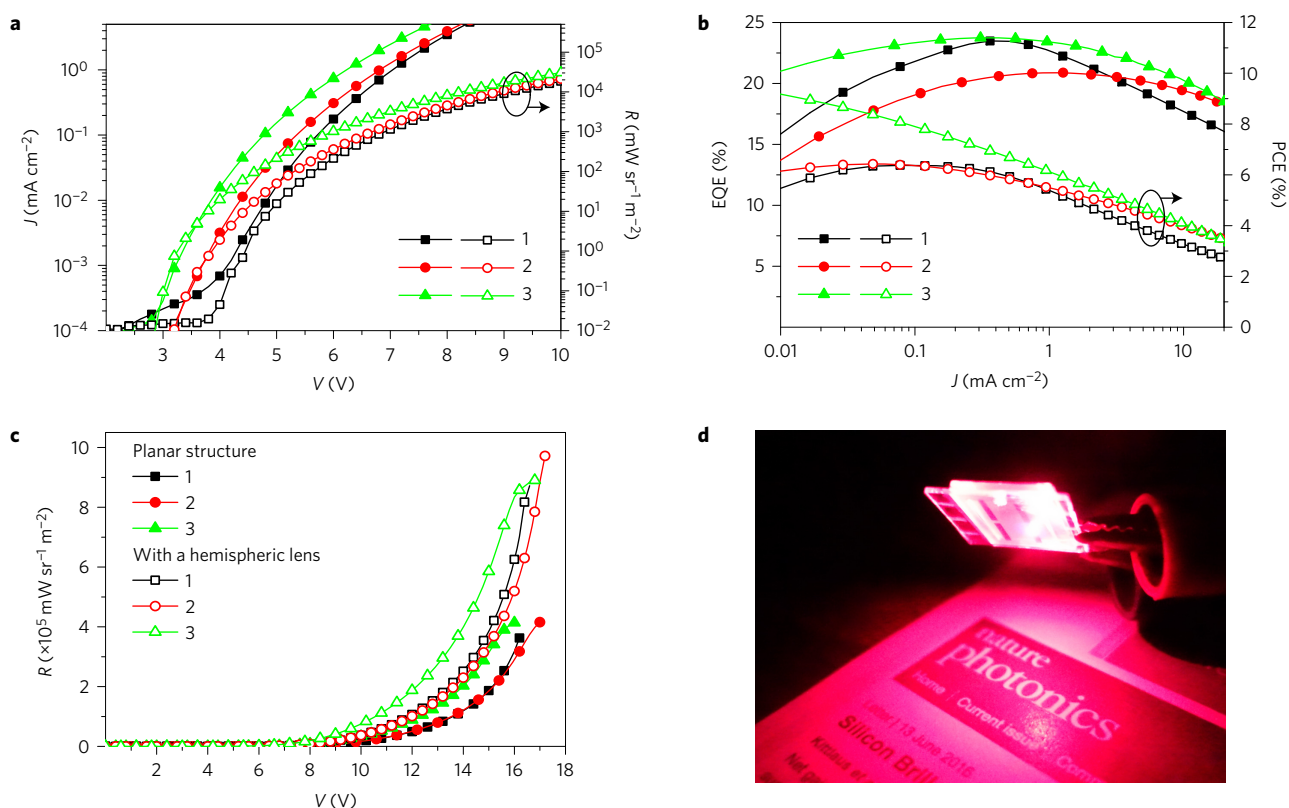


**Figure 4 | Device performance of optimized NIR OLEDs. a,  $J$ - $V$ - $R$  characteristics. b, EQE and PCE as a function of brightness. c, Maximum radiance with and without a hemisphere light out-coupling structure. d, Operation of the ~740 nm OLED using Pt(II) complex 1.**

increase in efficiency<sup>30,32</sup>. We thus integrated the OLEDs with a 1 cm diameter hemispheric lens. The detailed procedure is given in the Methods and the schematic diagram is depicted in the Supplementary Fig. 14. With the installment of the hemispheric lens, enhancement of the efficiency of the device was observed. EQEs of  $55 \pm 3\%$ ,  $46 \pm 2\%$  and  $51 \pm 3\%$  and PCEs of  $15 \pm 1\%$ ,  $15 \pm 1\%$  and  $21 \pm 1\%$  were measured for devices 1–3, respectively (see Supplementary Fig. 15). The corresponding maximum radiances obtainable for devices 1–3 were  $(3.6 \pm 0.2) \times 10^5$  mW sr<sup>-1</sup> m<sup>-2</sup>,  $(4.2 \pm 0.2) \times 10^5$  mW sr<sup>-1</sup> m<sup>-2</sup> and  $(4.1 \pm 0.2) \times 10^5$  mW sr<sup>-1</sup> m<sup>-2</sup> without the out-coupling hemisphere structure and  $(8.7 \pm 0.4) \times 10^5$  mW sr<sup>-1</sup> m<sup>-2</sup>,  $(9.7 \pm 0.5) \times 10^5$  mW sr<sup>-1</sup> m<sup>-2</sup> and  $(8.9 \pm 0.4) \times 10^5$  mW sr<sup>-1</sup> m<sup>-2</sup> with the out-coupling hemisphere structure, respectively (see Fig. 4c). The maximum radiance of device 1 is the highest reported to date in the NIR emission region (see Supplementary Table 8).

## Conclusion

Highly efficient NIR OLEDs were obtained using 2-pyrazinyl pyrazolate Pt(II) complexes 1–3. The photophysical data, GIWAXS, angle-dependent luminescence and computational approach revealed an ordered solid-state packing arrangement, as highlighted by the edge-on preferred orientation in the vacuum-evaporated thin films, which contributed to the intense NIR emission observed. For complex 1, the peak emission wavelength at ~740 nm and the PLQY of up to 81% are due to the exciton-like emission among the molecular aggregate and along the  $d_{z^2}$  orbital, which greatly suppresses exciton–optical phonon coupling. We attained OLEDs with a peak emission at 740 nm, an EQE of  $24 \pm 1\%$  and maximum radiance of  $(3.6 \pm 0.2) \times 10^5$  mW sr<sup>-1</sup> m<sup>-2</sup> using complex 1. The light out-coupling hemisphere structure further increased the EQE up to  $55 \pm 3\%$ . Both parameters are the highest reported values among NIR OLEDs.

## Methods

Methods and any associated references are available in the [online version of the paper](#).

Received 30 June 2016; accepted 17 October 2016; published online 28 November 2016

## References

- Pansare, V. J., Hejazi, S., Faenza, W. J. & Prud'homme, R. K. Review of long-wavelength optical and NIR imaging materials: contrast agents, fluorophores, and multifunctional nano carriers. *Chem. Mater.* **24**, 812–827 (2012).
- Stender, B., Völker, S. F., Lambert, C. & Pflaum, J. Optoelectronic processes in squaraine dye-doped OLEDs for emission in the near-infrared. *Adv. Mater.* **25**, 2943–2947 (2013).
- Borek, C. *et al.* Highly efficient, near-infrared electrophosphorescence from a Pt–metalloporphyrin complex. *Angew. Chem. Int. Ed.* **46**, 1109–1112 (2007).
- Guo, Z., Park, S., Yoon, J. & Shin, I. Recent progress in the development of near-infrared fluorescent probes for bioimaging applications. *Chem. Soc. Rev.* **43**, 16–29 (2014).
- Anzengruber, F., Avci, P., de Freitas, L. F. & Hamblin, M. R. T-cell mediated anti-tumor immunity after photodynamic therapy: why does it not always work and how can we improve it? *Photochem. Photobiol. Sci.* **14**, 1492–1509 (2015).
- Wang, S. *et al.* Highly efficient near-infrared delayed fluorescence organic light emitting diodes using a phenanthrene-based charge-transfer compound. *Angew. Chem. Int. Ed.* **54**, 13068–13072 (2015).
- Lu, H. *et al.* Highly efficient far red/near-infrared solid fluorophores: aggregation-induced emission, intramolecular charge transfer, twisted molecular conformation, and bioimaging applications. *Angew. Chem. Int. Ed.* **55**, 155–159 (2016).
- Xiang, H., Cheng, J., Ma, X., Zhou, X. & Chruma, J. J. Near-infrared phosphorescence: materials and applications. *Chem. Soc. Rev.* **42**, 6128–6185 (2013).
- Siebrand, W. Radiationless transitions in polyatomic molecules. II: triplet-ground-state transitions in aromatic hydrocarbons. *J. Chem. Phys.* **47**, 2411–2422 (1967).
- Englman, R. & Jortner, J. The energy gap law for radiationless transitions in large molecules. *Mol. Phys.* **18**, 145–164 (1970).
- Tong, C. C. & Hwang, K. C. Enhancement of OLED efficiencies and high-voltage stabilities of light-emitting materials by deuteration. *J. Phys. Chem. C* **111**, 3490–3494 (2007).

12. Prabhath, M. R. R., Romanova, J., Curry, R. J., Silva, S. R. P. & Jarowski, P. D. The role of substituent effects in tuning metallophilic interactions and emission energy of bis-4-(2-pyridyl)-1,2,3-triazoloplatinum(II) complexes. *Angew. Chem. Int. Ed.* **54**, 7949–7953 (2015).
13. Li, K. *et al.* Highly phosphorescent platinum(II) emitters: photophysics, materials and biological applications. *Chem. Sci.* **7**, 1653–1673 (2016).
14. Escudero, D. & Thiel, W. Exploring the triplet excited state potential energy surfaces of a cyclometalated Pt(II) complex: is there non-Kasha emissive behavior? *Inorg. Chem.* **53**, 11015–11019 (2014).
15. Adams, C. J., Fey, N. & Weinstein, J. A. Near-infrared luminescence from platinum(II) diimine compounds. *Inorg. Chem.* **45**, 6105–6107 (2006).
16. Bennett, M. A. *et al.* Unprecedented near-infrared (NIR) emission in diplatinum(III) ( $d^7-d^7$ ) complexes at room temperature. *J. Am. Chem. Soc.* **132**, 7094–7103 (2010).
17. Rossi, E. *et al.* Cyclometalated platinum(II) complexes of 1,3-di(2-pyridyl) benzenes: tuning excimer emission from red to near-infrared for NIR-OLEDs. *J. Mater. Chem.* **21**, 15501–15510 (2011).
18. Nguyen, M.-H. & Yip, J. H. K. Pushing pentacene-based fluorescence to the near-infrared region by platination. *Organometallics* **30**, 6383–6392 (2011).
19. Wu, X. *et al.* Highly efficient near-infrared emission from binuclear cyclometalated platinum complexes bridged with 5-(4-octyloxyphenyl)-1,3,4-oxadiazole-2-thiol in PLEDs. *Org. Electron.* **13**, 932–937 (2012).
20. Reid, E. F., Cook, V. C., Wilson, D. J. D. & Hogan, C. F. Facile tuning of luminescent platinum(II) Schiff base complexes from yellow to near-infrared: photophysics, electrochemistry, electrochemiluminescence and theoretical calculations. *Chem. Eur. J.* **19**, 15907–15917 (2013).
21. Zems, Y., Moiseev, A. G. & Perepichka, D. F. Convenient synthesis of a highly soluble and stable phosphorescent platinum porphyrin dye. *Org. Lett.* **15**, 5330–5333 (2013).
22. Nisic, F. *et al.* Platinum(II) complexes with cyclometalated 5- $\pi$ -delocalized-donor-1,3-di(2-pyridyl)benzene ligands as efficient phosphors for NIR-OLEDs. *J. Mater. Chem. C* **2**, 1791–1800 (2014).
23. Klaus, D. R., Keene, M., Silchenko, S., Berezin, M. & Gerasimchuk, N. 1D polymeric platinum cyanoximate: a strategy toward luminescence in the near-infrared region beyond 1000 nm. *Inorg. Chem.* **54**, 1890–1900 (2015).
24. Ku, H.-Y. *et al.* Luminescent Pt(II) complexes bearing dual isoquinolinyl pyrazolates: fundamentals and applications. *Dalton Trans.* **44**, 8552–8563 (2015).
25. Łapok, Ł. *et al.* Near infrared phosphorescent, non-oxidizable palladium and platinum perfluoro-phthalocyanines. *ChemPhysChem* **17**, 1123–1135 (2016).
26. Zhang, Y.-M. *et al.* Achieving near-infrared emission in platinum(II) complexes by using an extended donor-acceptor-type ligand. *Dalton Trans.* **45**, 5071–5080 (2016).
27. Cocchi, M., Kalinowski, J., Virgili, D. & Williams, J. A. G. Excimer-based red/near-infrared organic light-emitting diodes with very high quantum efficiency. *Appl. Phys. Lett.* **92**, 113302 (2008).
28. Graham, K. R. *et al.* Extended conjugation platinum(II) porphyrins for use in near-infrared emitting organic light emitting diodes. *Chem. Mater.* **23**, 5305–5312 (2011).
29. Kim, K.-H. *et al.* Crystal organic light-emitting diodes with perfectly oriented non-doped Pt-based emitting layer. *Adv. Mater.* **28**, 2526–2532 (2016).
30. Reineke, S. *et al.* White organic light-emitting diodes with fluorescent tube efficiency. *Nature* **459**, 234–238 (2009).
31. Wang, Z. B. *et al.* Unlocking the full potential of organic light-emitting diodes on flexible plastic. *Nat. Photon.* **5**, 753–757 (2011).
32. Lu, C.-Y. *et al.* Achieving above 60% external quantum efficiency in organic light-emitting devices using ITO-free low-index transparent electrode and emitters with preferential horizontal emitting dipoles. *Adv. Funct. Mater.* **26**, 3250–3258 (2016).
33. Chang, S.-Y. *et al.* Blue-emitting platinum(II) complexes bearing both pyridylpyrazolate chelate and bridging pyrazolate ligands: synthesis, structures, and photophysical properties. *Inorg. Chem.* **46**, 11202–11212 (2007).
34. Huang, Y.-C. *et al.* Insight into evolution, processing and performance of multi-length-scale structure in planar heterojunction perovskite solar cell. *Sci. Rep.* **5**, 13657 (2015).
35. Chang, S.-Y. *et al.* Platinum(II) complexes with pyridyl azolate-based chelates: synthesis, structural characterization, and tuning of photo- and electrophosphorescence. *Inorg. Chem.* **45**, 137–146 (2006).
36. Kaska, M., Rawls, H. R. & El-Bayoumi, M. A. The exciton model in molecular spectroscopy. *Pure Appl. Chem.* **11**, 371–392 (1965).
37. Pieper, J. *et al.* Excitonic energy level structure and pigment-protein interactions in the recombinant water-soluble chlorophyll protein. I. Difference fluorescence line-narrowing. *J. Phys. Chem. B* **115**, 4042–4052 (2011).
38. Lin, C.-L., Cho, T.-Y., Chang, C.-H. & Wu, C.-C. Enhancing light outcoupling of organic light-emitting devices by locating emitters around the second antinode of the reflective metal electrode. *Appl. Phys. Lett.* **88**, 081114 (2006).
39. Lin, C.-L., Chang, H.-C., Tien, K.-C. & Wu, C.-C. Influences of resonant wavelengths on performances of microcavity organic light-emitting devices. *Appl. Phys. Lett.* **90**, 071111 (2007).

### Acknowledgements

This research was supported by the Ministry of Science and Technology of Taiwan. We also thank the National Center for High-performance Computing (NCHC) for the computer time and facilities.

### Author contributions

K.T.L. conducted the synthesis and characterization of the Pt(II) complexes. R.-W.C.-C. executed the OLED fabrication and photophysical measurements. H.-W.L. designed the OLED structures, analysed the solid-state and OLED data and prepared the manuscript. Y.-J.S. did the optical modelling and simulations. S.-H.L. performed the computational calculations. P.-T.C. developed the theoretical approach, interpreted the photophysics and prepared the manuscript. C.-S.T. and Y.-C.H. conducted the GIWAXS measurements and analysed the data. Y.C. designed the Pt(II) complexes and prepared the manuscript. All authors discussed the results and contributed to the paper.

### Additional information

Supplementary information is available in the [online version of the paper](#). Reprints and permissions information is available online at [www.nature.com/reprints](http://www.nature.com/reprints). Correspondence and requests for materials should be addressed to H.-W.L., P.-T.C. and Y.C.

### Competing financial interests

The authors declare no competing financial interests.

## Methods

**General procedure for synthesis.** All reactions were performed under a nitrogen atmosphere. Solvents were distilled from appropriate drying agents before use. Commercially available reagents were used without further purification. The 5-(2-pyrazinyl)-3-trifluoromethylpyrazole, (fprpz)H, was synthesized via condensation of 2-acetylpyrazine with ethyl trifluoroacetate, followed by cyclization with hydrazine hydrate in ethanol. The Pt(II) metal intermediates, with the general formula [Pt(LH)Cl<sub>2</sub>] (LH = fppzH (2-pyridyl pyrazole) and tbfppzH (2-(4-*t*-butylpyridyl) pyrazole)), were prepared<sup>33</sup> from the reaction of stoichiometric amount of K<sub>2</sub>PtCl<sub>4</sub> and pyrazole in presence of HCl<sub>(aq)</sub>. Mass spectra were obtained on a JEOL AccuTOF GCX instrument operating in fast atom bombardment (FAB) mode. <sup>1</sup>H and <sup>19</sup>F NMR spectra were recorded on a Bruker DMX-600 instrument. The elemental analysis was carried out with a Heraeus CHN-O Rapid Elementary Analyzer.

**Synthesis of Pt(II) complexes.** The homoleptic 2-pyrazinyl pyrazolate Pt(II) complex was synthesized from the reaction of Pt(DMSO)<sub>2</sub>Cl<sub>2</sub> with two equivalents of 2-pyrazinyl pyrazole (e.g. fprpzH) in the presence of Na<sub>2</sub>CO<sub>3</sub> (3 equation.) and THF solvent. Alternatively, the heteroleptic pyrazinyl pyrazolate Pt(II) complexes were synthesized using an equal ratio of Pt(LH)Cl<sub>2</sub> and 2-pyrazinyl pyrazole in refluxing 2-methoxyethanol for 16 h. After being cooled to room temperature, the solvent was evaporated under a vacuum and the residue was filtered, washed with water and ethyl ether in sequence, then sublimed to yield the products. All complexes showed relatively good solubility in THF and toluene compared with other common organic solvents such as acetone, CH<sub>2</sub>Cl<sub>2</sub> and DMSO.

[Pt(fprpz)<sub>2</sub>] (1): dark-green powder, yield: 93%. mass spectral (MS) data (FAB, <sup>195</sup>Pt): mass/charge (*m/z*) ratio 621.1 [M<sup>+</sup>]; <sup>1</sup>H NMR (600 MHz, d<sub>8</sub>-THF, 323 K): δ 10.37 (d, *J* = 3 Hz, 2H), 9.20 (s, 2H), 8.72 (d, *J* = 3 Hz, 2H), 7.19 (s, 2H); <sup>19</sup>F NMR (564 MHz, d<sub>8</sub>-THF, 323 K): δ -61.86 (s, 6F). Combustion elemental analysis for C<sub>16</sub>H<sub>8</sub>F<sub>6</sub>N<sub>8</sub>Pt: C, 30.93; H, 1.30; N, 18.03. Found: C, 31.08; H, 1.62; N, 17.82.

[Pt(fprpz)(fppz)] (2): red powder, yield: 73%. MS (FAB, <sup>195</sup>Pt): *m/z* 620.1 [M<sup>+</sup>]; <sup>1</sup>H NMR (600 MHz, d<sub>8</sub>-THF, 323 K): δ 10.42 (d, *J* = 3.5 Hz, 1H), 10.40 (d, *J* = 6.3 Hz, 1H), 9.12 (s, 1H), 8.63 (d, *J* = 3.5 Hz, 1H), 8.06 (t, *J* = 9.1 Hz, 1H), 7.83 (d, *J* = 9.1 Hz, 1H), 7.44 (t, *J* = 6.3 Hz, 1H), 7.11 (s, 1H), 6.98 (s, 1H); <sup>19</sup>F NMR (564 MHz, d<sub>8</sub>-THF, 323 K): δ -61.71 (s, 3F), -61.76 (s, 3F). Combustion elemental analysis for C<sub>17</sub>H<sub>9</sub>F<sub>6</sub>N<sub>7</sub>Pt: C, 32.91; H, 1.46; N, 15.80. Found: C, 32.93; H, 1.64; N, 15.91.

[Pt(fprpz)(tbfppz)] (3): red powder, yield: 76%. MS (FAB, <sup>195</sup>Pt): *m/z* 677.6 [M<sup>+</sup>]; <sup>1</sup>H NMR (600 MHz, d<sub>8</sub>-THF, 323 K): δ 10.37 (d, *J* = 3.6 Hz, 1H), 10.23 (d, *J* = 6.6 Hz, 1H), 9.20 (d, *J* = 1.8 Hz, 1H), 8.69 (d, *J* = 3.6 Hz, 1H), 7.93 (d, *J* = 1.8 Hz, 1H), 7.61 (d, *J* = 6.6 Hz, 1H), 7.19 (s, 1H), 7.13 (s, 1H), 1.44 (s, 9H); <sup>19</sup>F NMR (564 MHz, d<sub>8</sub>-THF, 323 K): δ -61.63 (s, 3F), -61.70 (s, 3F). Combustion elemental analysis for C<sub>21</sub>H<sub>17</sub>F<sub>6</sub>N<sub>7</sub>Pt: C, 37.28; H, 2.52; N, 14.49. Found: C, 37.60; H, 2.68; N, 14.04.

**Thin-film fabrication.** The 18 nm thin films of the Pt(II) complexes were deposited on fused silica substrates under a pressure of  $2 \times 10^{-6}$  torr. The deposition rate of the Pt(II) complex layers was 0.1 nm s<sup>-1</sup>. All of the tooling factors were calibrated by a surfcoorder (ET200, Kosaka Laboratory Ltd).

**Absorption, PL spectra and PLQY measurements.** Absorption spectra were measured by using an ultraviolet-visible spectrophotometer (UV2600, Shimadzu) and the PL spectra were measured with a He-Cd laser ( $\lambda = 325$  nm, Melles Griot) excitation, and the emission was detected by using a CCD (charge-coupled device) camera (PIXIS 256BR, Princeton Instruments). The absolute PLQY was recorded by the same system incorporating an integrating sphere and calculated following the procedures outlined in the literature<sup>40</sup>. All of the optical measurements were performed in an inert atmosphere to avoid water and oxygen.

**Time-resolved PL measurement.** Time-resolved PL was measured by using a pulsed frequency tripled Nd:YAG laser ( $\lambda = 355$  nm, Minilite Series, Continuum) as an excitation source and a photon-counting photomultiplier tube (PMT) as a detector. The measured films were deposited on fused silica substrates with a film thicknesses of 200 nm. The whole measurement sequence was performed under an inert environment.

**Angular-dependent PL measurement.** The orientation of the emission dipoles was analysed by measuring the angular-dependent PL intensity of the 30 nm thin films on fused silica substrate attached to a half-cylindrical lens and comparing the experimental results with the theoretical values derived from the classical dipole model and the transfer matrix method. The experimental set-up comprised a motorized rotation stage to control the receiving angle of emission from an optical fibre and a polarizer to collect the *P*-polarized emission. The detection wavelength

was selected at the emission peak wavelength of each sample by using a monochromator (Acton SpectraPro SP-2300, Princeton Instruments). The fibre-coupled light signals were accumulated by a PMT (PMC-100-1, Becker & Hickl GmbH). Excitation light from an He:Cd laser ( $\lambda = 325$  nm) was guided by mirrors to the sample with an incident angle of 135° to avoid collecting the laser beam with the optical fibre.

## GIWAXS/grazing-incidence small-angle X-ray scattering (GISAXS)

**measurement.** The measurement was performed at the BL23 beam line of the National Synchrotron Radiation Research Center (NSRRC), Taiwan. The studied thin films were deposited on the Si substrate. The GISAXS and GIWAXS patterns were simultaneously collected with different detectors during measurement. The incidence angle of monochromated X-ray beam was  $\sim 0.2^\circ$ . The reduced 1D GISAXS profiles were expressed as a function of the scattering vector *Q* along the in-plane direction (parallel film surface) covering the Yoneda peak. For morphological studies, the grain size of complex 2 is estimated to be  $\sim 60$  nm by GISAXS. In contrast, the grain sizes of 1 and 3 are larger than  $\sim 200$  nm, which is beyond the size detection limit of GISAXS (see Supplementary Fig. 1).

**Computational method.** All of the calculations were performed with the Gaussian 09 program package<sup>41</sup>. The geometry optimization of ground states of the studied Pt(II) complexes were simulated with DFT at the B3LYP/LANL2DZ (Pt) and B3LYP/6-31g(d,p) (H, C, N, F) levels using THF as the solvent. The optimized structures of the three Pt(II) complexes were then used to calculate the five lowest singlets (*S*<sub>0</sub> → *S*<sub>5</sub>) and triplet optical electronic transitions (*S*<sub>0</sub> → *T*<sub>5</sub>) using the TD-DFT method. The solvent effect is based on the polarizable continuum model (PCM), which is implemented in the Gaussian 09 program. We also studied the singlet and triplet excited states for both the dimer and trimer. We took the Mulliken population analysis (MPA) to obtain the electron density distribution of each atom in specific molecular orbital of the Pt(II) complexes and to calculate the MLCT and MMLCT in each assignment of the singlet and triplet optical transitions.

**Materials for OLED fabrication.** Organic materials NPB, MCP, TPBi and Liq were purchased from Nichem Fine Technology Co., Ltd. ITO glass substrates were purchased from Ruilong Co., Ltd.

**Device fabrication and characterization.** The OLEDs were fabricated on glass substrates with patterned 100 nm thick ITO. All of the thermal evaporation processes were executed under a pressure of  $2 \times 10^{-6}$  torr without breaking the vacuum. Before the deposition of the organic layers, the ITO substrates were pre-cleaned with detergent followed by acetone and methanol and finally exposed to ultraviolet ozone for 5 min. The deposition rates of organic layers were  $\sim 0.1$  nm s<sup>-1</sup>.

For the light out-coupling on OLEDs, samples were attached to a half-cylinder lens with index-matching oil then excited by an He:Cd laser source. The angular-dependent emission was collected by photomultiplier tubes.

A programmable source measurement unit (2636B, Keithley) was used as a driving source of the device while the light intensity was measured by a calibrated integrating sphere system (Labsphere) with a fast response silicon detector according to standard procedures<sup>42</sup>. The deviation of the devices leads to a variation in the area of  $\pm 2\%$  due to the shadow effect of the vacuum thermal evaporation. The current and voltage values were estimated to have an accuracy of 0.015% and 0.025%, respectively, which were negligible compared with other factors. The luminance was calibrated with a NIST traceable meter (OPHIR) with a  $\pm 3\%$  accuracy across the wavelength range of 270–950 nm and confirmed with a spectroradiometer (Photo Research PR-655) with a  $\pm 2\%$  accuracy in the visible region. Accuracy after the consideration of both the variation in the device area and the instrumental accuracy was estimated to be around  $\pm 5\%$ .

All OLED devices were mounted on the north pole aperture of the integrating sphere for all measurements. The diameter of the integrating sphere was 3.3 inch and the diameter of the aperture was 0.5 inch. To extract the substrate modes out of the device, a 1 cm diameter BK7 half-sphere lens was attached to the substrate using an index-matching oil ( $n = 1.51$ ).

## References

- De Mello, J. C., Wittmann, F. H. & Friend, R. H. An improved experimental determination of external photoluminescence quantum efficiency. *Adv. Mater.* **9**, 230–232 (1997).
- Frisch, M. J. *et al.* *Gaussian 09 Revision D.01* (Gaussian Inc., 2013).
- Forrest, S. R., Bradley, D. C. & Thompson, M. E. Measuring the efficiency of organic light-emitting devices. *Adv. Mater.* **15**, 1043–1048 (2003).